OPEN ACCESS
IOP Publishing
Plasma Sources Science and Technology
Plasma Sources Sci. Technol. **34** (2025) 125007 (18pp)
https://doi.org/10.1088/1361-6595/ae2208

EUV-induced low pressure hydrogen and H_2/Sn plasmas

Tugba Piskin[1,2], Vladimir Volynets[3], Hyunjae Lee[3], Sang Ki Nam[3] and Mark J Kushner[2,*]

[1] Lam Research Corporation, 11261 SW Leveton Dr, Tualatin, OR 97065, United States of America
[2] Electrical Engineering and Computer Science Department, University of Michigan, 1301 Beal Ave., Ann Arbor, MI 48109-2122, United States of America
[3] Mechatronics Research, Samsung Electronics Co. Ltd, 1-1 Samsungjeonja-ro, Hwaseong-si, Gyeonggi-do 18448, Republic of Korea

E-mail: mjkush@umich.edu, tugba.piskin@lamresearch.com, hj0928.lee@samsung.com and sangki.j.nam@samsung.com

Received 4 September 2025, revised 29 October 2025
Accepted for publication 20 November 2025
Published 12 December 2025

Abstract

The continuing decrease in feature size in microelectronics fabrication has been enabled by a progressive decrease in the wavelengths for photolithography. The recent deployment of extreme ultra-violet (EUV) lithography systems with photon wavelengths centered at 13.5 nm has enabled feature sizes below 10 nm. One method to produce EUV photon fluxes is to ablate and ionize tin droplets with pulsed lasers. A possible consequence of the ablation is that the resulting tin vapor may coat optical components. By filling the chamber with low-pressure H_2 gas that does not significantly absorb the EUV photons, a low-density plasma is produced by the EUV photon flux that dissociates and ionizes the hydrogen. Tin films on optics can then be etched by H atoms and ions producing stannane (SnH_4), which can then be pumped away. In this paper, results from a computational investigation of the plasma formation that occurs by EUV photon fluxes (13.5 nm, 92 eV) passing through low pressure H_2 and tin vapor are discussed. Electron energy distributions produced by the photo-generated primary electrons and the resulting plasma densities are discussed as a function of the background gas pressure, metal vapor and pulse power format.

Keywords: EUV produced plasma, simulation, particle distribution functions, hydrogen and tin plasmas

1. Introduction

The progressive decrease in feature size in microelectronics fabrication has been enabled by a reduction of the wavelengths used in photolithography. The current generation of microelectronics devices are now sub-10 nm, with dimensions approaching a few nm [1–3]. This capability follows from the progressive decrease in lithography wavelengths from those produced by Hg lamps (436 nm, 365 nm) [4] and deep-ultra-violet excimer lasers (KrF 248 nm, ArF 193 nm [5, 6] and F_2 157 nm [7]). Photolithography using 193 nm systems dominated to feature sizes as small as 10 nm by using optical proximity correction, high index immersion techniques and multiple patterned exposure [8]. With there being limits to these techniques, shorter wavelength sources were pursued.

Extreme ultra-violet (EUV) photolithography tools have been critical to the transition to sub-10 nm features [8, 9]. Xenon and lithium plasmas were investigated as sources of EUV photons, however the conversion efficiency (the ratio of emitted EUV power to input power) was lower than desired

* Author to whom any correspondence should be addressed.

[10–12]. The first systems to be implemented in high volume manufacturing generate EUV photons by laser ablation of tin (Sn) droplets [13, 14]. In this system, photons having a wavelength centered at 13.5 nm (92 eV) are emitted from the resulting tin plasma [15]. These systems continue to be improved through introduction of higher performing photoresist and reflective optics for EUV photons, and higher efficiency and more stable photon sources to increase wafer per hour production rates [10, 16–19].

The operation of the current generation of EUV lithography systems is briefly summarized. Liquid tin droplets having a diameter of ≈20–30 μm are generated at repetition rates of 50 −60 kHz and injected into a hydrogen filled chamber. The droplets are flattened and then ablated by a pulsed CO_2 laser having pulse lengths of tens of ns and powers of 20–30 kW [18, 20, 21]. The EUV photons emitted by the laser-produced plasma are directed by a Bragg reflection collector mirror for delivery to the intermediate focus (IF), and transport to the scanner exposing the wafer. Multilayer Bragg reflector Mo/Si mirrors were developed with multiple filters to reflect EUV photons and refract other radiation, producing a theoretical limit of reflection at 13.5 nm of about 70% [13, 22]. The average power at 13.5 nm at the IF of up to 500–600 W enables several hundred wafers per hour, WPH, throughput [22–24].

One of the challenges in maintaining high power levels to the IF is degradation of the reflectivity of the collector mirror due to contamination by debris from the ablated Sn droplet. Low energy Sn atoms and ions (several eV) can deposit on the mirror decreasing reflectivity [25]. High energy tin ions (several keV) can sputter and implant into the optics' surface [26]. A 1 nm Sn surface coverage (approximately 4 Sn atoms) can produce a decrease in reflectivity up to 10% [27]. The use of a buffer gas in the chamber has been investigated to reduce the flux of tin atoms and ions onto the optics. By flowing the gas through the chamber, ambient Sn atoms and debris can be removed from the chamber. The ideal buffer gas would not significantly absorb either the CO_2 laser that ablates the Sn droplet or the resulting EUV photons, and would slow energetic tin radicals and ions, while cleaning the chamber and collector surfaces *in situ*. Klunder *et al* found that the deposition of atomic-tin debris was significantly reduced using an argon buffer gas of pressures 1–10 Pa (7.5–75 m Torr) [27]. Hydrogen gas, having a high EUV transmission, thermal conductivity, and specific heat capacity, is another favored buffer gas [10, 25].

Although moderate pressures of H_2 are largely transparent to the EUV flux, EUV photons passing through the H_2 will ionize and dissociate the hydrogen gas. The resulting hydrogen plasma, then produces fluxes of hydrogen ions and radicals to plasma facing materials. In addition to the H_2 buffer gas slowing fast tin atoms and ions produced by Sn ablation through gas phase collisions, these fluxes of H atoms and ions can remove deposited tin on surfaces by producing stannane, SnH_4 [27–31]. Stannane is a volatile gas that can be removed from the chamber by pumping, though also may redeposit on surfaces [10, 25]. Optimizing the EUV induced hydrogen plasma can enable debris mitigation and collector cleaning while minimizing detrimental effects. For example, energetic hydrogen ions can produce blisters in optical surfaces [32].

EUV induced plasmas have been investigated by several researchers [33]. Astahkov *et al* measured the electron density and simulated EUV induced hydrogen and argon plasmas in a microwave resonant cavity [34]. The EUV was produced by a xenon discharge source producing wavelengths of 10–18 nm (70–120 eV). They found that plasma densities increase with pressure (1 Pa—10 Pa). The plasma density was as high as 1.8×10^9 cm^{-3} in argon and as high as 1×10^8 cm $^{-3}$ in hydrogen. They found that early during the EUV photon pulse energetic electrons generated by photoionization can escape the plasma, resulting in net positive space charge. The net positive space charge can then produce a large plasma potential. On the other hand, photo-electron emission from surfaces by the EUV radiation introduces negative space charge near boundaries that can reduce plasma potential in those regions.

Ion energy distributions striking surfaces from EUV induced plasmas were investigated at a pressure of 5 Pa (37.5 m Torr) of H_2 at a repetition rate of 500 Hz [35]. The EUV was produced by a xenon discharge. H^+, H_2^+ and H_3^+ were detected with energies up to 20 eV. Mao *et al* numerically investigated EUV (13.5 nm) induced plasma in hydrogen gas at 1–5 Pa, using a particle-in-cell (PIC) simulation [36]. They found that the electric fields distributions in the plasma were sensitive to the secondary electron emission from surfaces by photon and electrons. Tin etching by hydrogen plasmas was experimentally investigated using plasma sources other than EUV [37]. Depending on the hydrogen radical densities and ion energies from the hydrogen plasma sources, etch rates varied from a few to hundreds nm min^{-1} [37–39].

In this paper we discuss results from a numerical investigation of EUV (13.5 nm) induced hydrogen plasmas using a geometry that is notionally based on commercial EUV lithography systems which use laser ablation of Sn droplets. Electron energy distributions (EEDs) produced by the energetic electrons resulting from photoionization and the resulting plasma properties are discussed. The operating conditions and geometry for the simulations were chosen to enable the computations to be tractable and to enable investigation of the fundamental plasma properties while also being relevant to commercial EUV systems. The hydrogen gas pressure ranged from 5 Pa to 100 Pa (37.5–750 m Torr) with EUV pulses at 3.3 MHz with pulse lengths of 60 ns, and peak power of 5 kW. EUV pulses at 50 kHz, 1 μs pulse length and 15 kW power were also investigated. Plasmas produced in pure H_2 and H_2 with Sn vapor were investigated.

We found that depending on conditions, EUV plasma formation is approximately half due to the initial photoionization by the EUV radiation, and half due to the slowing of the energetic photoelectrons produced in that process. The slowing of these energy energetic electrons may take hundreds of ns to a few microseconds, thereby contributing ionization and space charge to additional plasma produced by the next EUV pulse. The chamber averaged EUV induced plasma density scales

nearly linearly with gas pressure early in the pulse train. The loss of energetic photo-electrons early in the EUV pulse contributes to positive space charge and a spike in plasma potential of up to 100 V which diminishes with successive pulses. Secondary photo-electron emission from surfaces alters the plasma potentials near surfaces during the startup process, in some cases producing a negative plasma potential which diminishes with plasma buildup in the chamber.

The numerical and physics models are described in section 2. Properties of EUV produced plasmas predicted by the simulations are discussed in section 3 for pure H_2 plasmas and in section 4 for H_2/Sn mixtures. Plasma properties for conditions commensurate with commercial EUV sources are discussed in section 5. Concluding remarks are in section 6.

2. Description of the model

These numerical investigations were conducted with the Hybrid Plasma Equipment Model (HPEM) [40], a modeling platform developed for low pressure plasma processing reactors as used for semiconductor fabrication. Since detailed descriptions of the HPEM are available elsewhere [41, 42] only a brief description is provided here, including the updates to capture the physics of EUV-induced plasmas.

The HPEM consists of modules that address different classes of physics and which exchange information using time slicing techniques. The modules used in this investigation are the Fluid Kinetics-Poisson Module (FKPM), the Electron Energy Transport Module (EETM) and the Photon Transport Module (PTM). In the FKPM continuity, momentum and energy conservation equations and Poisson's equation are integrated in a coupled manner to obtain densities, temperatures, and fluxes of charged and neutral species, and electrostatic potential. These quantities include properties of the bulk electrons that have average energies of less than several eV. These values are transferred to the EETM in which time and spatially dependent EEDs for high energy electrons produced in the volume and secondary electrons emitted from surfaces are generated using Monte Carlo methods. The source of the high energy electrons in the volume is photoionization by the EUV beam. The source of secondary electrons are photo-electron emission and secondary emission by ion and electron impact. The EEDs are used to produce electron impact rate coefficients. High energy electrons slowing to thermal energies are then used as source functions in the continuity equation for bulk electrons. These quantities are transferred to the FKPM.

Transport of EUV photons and photoionization sources are computed in the PTM using Monte Carlo techniques. To emulate the EUV source produced by ablation of the Sn droplet, photon, pseudoparticles representing EUV photons are isotropically launched from the center of the reactor (location $\vec{r}$) over a diameter of 30 μm with an intensity weighting $I_{\rm wi}$ (photons s^{-1}) in proportion to the number of photons emitted from that cell during that particular call to the PTM. The intensity weighting of the particle is diminished along its straight-line trajectory in accordance with the local absorption that occurs. The intensity weighting of $I_{\rm wi}$ at location $\vec{r}'$ due to photons produced at $\vec{r}$

$$I_{\rm wi}\left(\vec{r}'\right) = I_{\rm wi}\left(\vec{r}\right)\exp\left(\int_{\vec{r}}^{\vec{r}'}\sum_k N_k\left(\vec{r}''\right)\sigma_k {\rm d}\vec{r}''\right) \tag{1}$$

where N_k is the density of absorbing species having absorption cross section σ_k. The photoionization source of species k having density N_k is then

$$S_k\left(\vec{r}'\right) = I_{\rm wi}\left(\vec{r}'\right)N_k\left(\vec{r}'\right)\sigma_{ki} \tag{2}$$

where σ_{ki} is the ionization cross section for species k. The photons are tracked until they are either fully absorbed (which is not the case for these conditions) or strike a surface. Photons striking a reflecting surface are redirect with an intensity weighting scaled by the reflectivity of the mirror. Photons striking surfaces having a photo-electron emission probability, produce sources of secondary electrons that are used as input in the EETM.

The photoionization reactions for 13.5 nm photons included in the model are in table 1. For 13.5 nm photons having an energy of 92 eV, the cross section for single photoionization of molecular hydrogen is the dominant process having a cross section of 4.9×10^{-20} cm^2, or 78% of all photoionization processes for H_2 [43, 44]. The photo-electron is isotropically emitted with an energy of 76.6 eV. Dissociative photoionization with a cross section of 1.1×10^{-20} cm^2, corresponding to 18% of the photoionization reactions, produces an intermediate unstable H_2^{+*} which dissociates essentially immediately into H^+ and H [43, 44]. The photo-electron carries away 32 eV. The resulting hydrogen ion and atom emerge from the dissociative ionization with 16 eV of kinetic energy due to Franck–Condon heating [44]. The kinetic energy of the heavy particle fragments is included as source terms in the energy equations of H and H^+ in the FKPM. The double photoionization reaction has a cross section of 2.8×10^{-21} cm^2 [45, 46] which represents about 4% of the total photo-electron production. The photo-electrons share 40 eV of kinetic energy. The H_2^{2+} dissociates immediately producing two H^+ which each emerge with 9.4 eV of kinetic energy. The photoionization cross section of H was estimated to be half that of H_2. With Sn vapor in the chamber, photoionization of Sn also occurs with a cross section of 1.1×10^{-17} cm^2, producing a photoelectron having an energy of 84.5 eV [47]. The photoionization cross section of Sn is about 170 times that of the total photoionization cross section for H_2.

The HPEM was updated to capture the high energy and non-local transport of electrons resulting from photoionization reactions and by photo-electron emission. In the options used in this investigation, trajectories of electrons produced by secondary emission processes are kinetically tracked in the EETM using Monte Carlo techniques with acceleration

Table 1. Photoionization reactions of hydrogen and tin with 92 eV photons.

Reaction	Electron heating ε_e (eV)	Gas heating ΔH (eV)	Cross section (cm^2)
$h\nu+H_2 \rightarrow H_2^+ + e$	76.6	—	4.9×10^{-20} [43, 44]
$h\nu+H_2 \rightarrow H^+ + H^* + e$	50	16	1.1×10^{-20} [43, 44]
$h\nu+H_2 \rightarrow 2H^+ + 2e$	40	18.8	2.8×10^{-21} [45, 46]
$h\nu + H \rightarrow H^+ + e$	78.4	—	2.45×10^{-19} [43, 44]
$h\nu + Sn \rightarrow Sn^+ + e$	84.5	—	1.1×10^{-17} [47]

provided by electric fields produced in the FKPM and collision probabilities using densities produced in the FKPM. The electron pseudoparticles are randomly released from surfaces in proportion to the flux of electrons, ions and photons incident onto the surface weighted by their secondary electron emission coefficients. To accommodate the electrons produced by EUV photoionization, the probability for launching pseudoparticles in the EETM was made

$$p(\vec{r}) = p_s(\vec{r}) + p_v(\vec{r}) \tag{3a}$$

$$p_s(\vec{r}) = \left(\sum_i \phi_i(\vec{r})\gamma_i(\vec{r}) + \phi_p(\vec{r})\gamma_p(\vec{r}) \right) dA(\vec{r}) \tag{3b}$$

$$p_v(\vec{r}) = \sum_{i,k} \phi_p(\vec{r}) N_i(\vec{r}) \sigma_{ik} dV(\vec{r}) \tag{3c}$$

where $p_s(\vec{r})$ is the incremental probability for launching secondary electrons from surface locations having area $dA(\vec{r})$ and $p_v(\vec{r})$ is the probability for launching photo-produced electrons from sites having volume $dA(\vec{r})$. In equation 3(b), ϕ_i is the flux of a gas phase species (ions and electrons) incident onto the surface having secondary electron emission coefficient γ_i, and ϕ_p is the EUV photon flux to that location having secondary emission coefficient γ_p. In equation 3(c), the summation is over gas species having density N_i and photoionization cross section σ_{ik}, allowing for there being several photoionization processes for each species. The secondary electron emission coefficient for all ions was 0.1.

The electron pseudoparticles for photoionization are emitted isotropically with the energies given in table 1. The energy spectrum of secondary electrons emitted from surfaces due to the high energy EUV photons is [48]:

$$P(\varepsilon_s) \sim \varepsilon_p \mu(\varepsilon_p) \frac{\varepsilon_s}{(\varepsilon_s + \Phi_w)^4} \tag{4}$$

where ε_s is the emitted electron energy, Φ_w is the work function of the material, ε_p is the energy of the incident photon energy, and μ is the absorption coefficient. Electrons are released with energies randomly chosen from this probability distribution. For surfaces having a work function of 4–5 eV, photo-emission by 13.5 nm photons produces electrons having energies of 1–6 eV. There is a high energy tail to the photo-emitted electrons that extends to above the excitation and ionization threshold energies of the gas. As a result, photo-emitted electrons from surfaces can produce excitation and ionization of the gas. The photoelectron yield (electrons per photon) significantly differs by material and cleanliness of the surface [36, 49]. After considering these issues, the photoelectron yield was chosen to be 0.03 for all surfaces.

With photoionization producing electrons with energies as large as 76.6 eV, secondary electron emission by energetic electrons is also a potentially important process. Probabilities for secondary electron emission induced by electron impact on the surfaces as a function of incident energy and angle were obtained from [50]. For example, surfaces with a ~4.5 eV work function, the secondary electron yields by 76.6 eV electrons are 0.48 for 60° from the normal and 0.52 for 30° from the normal incidence (where 90° is grazing).

Charging of dielectric surfaces that produce surface electric potentials is potentially an important process as there is, under usual operating conditions, no applied voltage. All metal surfaces were held at ground (zero) potential. The electric potential of dielectrics was determined by their charge density, which is included in the solution of Poisson's equation. The charge density is computed from

$$\frac{d\rho(\vec{r})}{dt} = \left[\sum_i q_i \left(S_i(\vec{r}) + S_e(\vec{r}) + \left(\frac{dN_i(\vec{r})}{dt} \right)_c - \nabla \cdot \phi_i(\vec{r}) \right) \right]_v + \left[\sum_i -\nabla \cdot q_i \phi_i(\vec{r}) + q_e(-\nabla \cdot \gamma_i \phi_i(\vec{r})) - q_e(-\nabla \cdot \gamma_p \phi_p(\vec{r})) - \nabla \cdot \sigma \vec{E} \right]_s \tag{5}$$

where the first bracketed terms refer to locations in the volume and the second bracket refers to locations on the surfaces and inside of materials. The sums are over charged species having charge q_i, where q_e is the charge on electrons. The time derivative of species densities includes all collisional processes, including photoionization. S_i represents sources due to non-collisional processes, such as the contribution of secondary electrons emitted from surfaces. The current through solid materials is represented by the last term, for material conductivity σ and electric field $\vec{E}$.

The HPEM operates in an iterative manner in which information is sequentially exchanged between modules. Here, the order of execution of the modules is: PTM, EETM, FKPM. For the results discussed here, the cycle time between modules was 5 ns, which is shorter than the slowing down time of photoelectrons in the gas. As a result, the space charge of the photoelectrons (both from the volume and surface) should be considered in the solution of Poisson's equation. The time history of the density of energetic pseudoparticles, produced by either surface or volume processes is recorded in the EETM

Table 2. Species in the mechanism.

H_2 Only:	$H_2, H_2^*, H_2(v=1), H_2(v=2), H_2(v=3)$, H, $H(n=2), H(n=3), H^+, H^-, H_2^+, H_3^+$, e
Sn addition:	
$Sn(^3P_0)$, $Sn(^3P_1)$, $Sn(^3P_2)$, $Sn(^1D_2)$, Sn*, Sn^+	

and interpolated in the following call to the FKPM to provide a charge density in solution of Poisson's equation. In doing so, the photoionization term (equation (5)) is only applied to the resulting ions in the FKPM. When energetic pseudo-particles fall in energy below the threshold value of 4 eV, their charge and densities are recorded and used as sources of thermal or bulk electrons. These sources are used in the FKPM in the electron continuity equation, in the charge density (term S_e in equation (5)) which is used in solution of Poisson's equation for electric potential, and as a power source in the electron energy transport equation. The energetic photoelectrons which have not yet fallen below this threshold energy are referred to as *in-flight* electrons.

With the exception of the addition of the photochemical processes, the H_2 plasma chemistry used here is essentially the same as described in [51]. The species included in the mechanism are listed in table 2. Three vibrationally excited H_2 levels are included with 0.516, 1.0 and 1.5 eV excitation energies. H_2^* is a lump state consisting of nominally $H_2(B^1\Sigma)$ and higher bound excited states. Although the negative H^- ion is included in the mechanism, the negative ion density is not significant in the range of operating conditions investigated in this study. Dissociative electron attachment to hydrogen ($e + H_2 \rightarrow H_2^- \rightarrow H + H^-$) has a threshold energy around 3.5 eV for the ground vibrational state. The maximum cross section is about 3.0×10^{-21} cm^{-2} [52] at 3.7 eV and decreases for higher energies. Although the threshold energy decreases and maximum cross section increases with higher vibrational excitation, the fractional densities of vibrationally excited H_2 are generally small [53]. (At the center of the reactor, vibrationally excited H_2 has a mole fraction of $<10^{-3}$.) As a result, dissociative electron attachment does not play an important role in the plasma kinetics.

With the goal of assessing the consequences of having metal vapor in the chamber, a reaction mechanism was developed for Sn atoms in the low temperature plasma environment. Electron impact excitation and ionization cross sections for Sn atoms were taken from Umer *et al* [54]. The Sn species included in the model are listed in table 2. Due to their large splitting, all 3 components of the ground state multiplets were included. The true ground state is $Sn(^3P_0)$ and its multiplets are $Sn(^3P_1)$ [0.21 eV] and $Sn(^3P_2)$ [0.44 eV]. The $Sn(^1D_2)$ [1.06 eV] was explicitly included whereas all higher excited states were combined into a lumped state Sn^* which energetically corresponds to $Sn(^1S_0)$ [2.35 eV]. Momentum transfer collisions were included for all Sn species as well as electron impact processes between the Sn species and electron impact ionization.

With the ionization potential of Sn being 7.34 eV, charge exchange reactions between all hydrogen species ions and Sn are energetically allowed. Charge exchange reactions of H_n^+ and neutral Sn species were included with a rate coefficient of 10% that of the Langevin value [55]. Using this approximation, the rate coefficient for charge exchange between H_2^+ and $Sn(^3P_0)$ is 2.8×10^{-10} cm^3 s^{-1}.

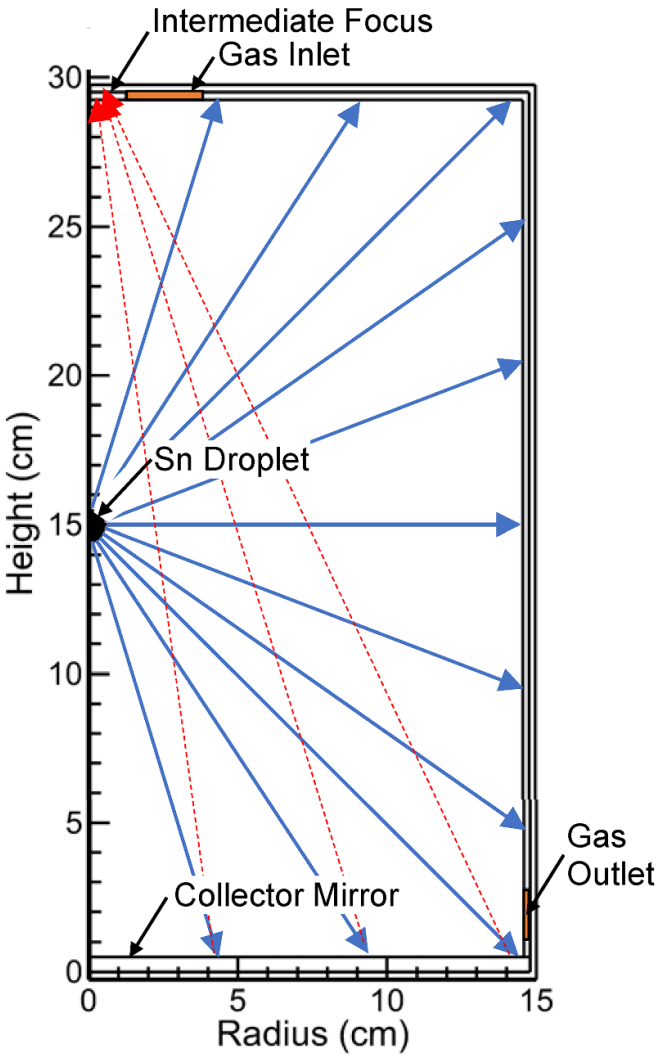

Figure 1. Geometry used in the simulation.

The geometry used in the simulation, shown in figure 1, is intended to resemble but not replicate commercial EUV plasma sources [23]. The cylindrically symmetric chamber is 30 cm in diameter and 30 cm tall. The Sn droplet and source of the EUV radiation is on axis at a height of 15 cm with the EUV radiation being emitted isotropically. The IF is on the symmetry axis on the top boundary having diameter of 2.4 cm, surrounded by the gas inlet having an outer diameter of 7.5 cm. The gas outlet is on the lower outer boundary. The boundary of the computational domain is grounded metal and is covered by conductive dielectric ($\sigma = 0.01$ S cm^{-1}). The bottom surface of the chamber is the collector mirror which redirects photons to the IF with a reflectivity of 0.97 (reduced by the photoelectron emission probability). Secondary emission by electrons, ions and photons occurs on all surfaces except for the IF, pump gas inlet and gas outlet.

3. Properties of EUV induced plasma in H_2

The base case operating conditions are a H_2 gas pressure of 10 Pa (75 m Torr) with an inlet flow rate of 2500 sccm and all bounding surfaces having a temperature of 325 K. The EUV pulse has a peak power of 5 kW and pulse length of 60 ns (rise and fall times of 20 ns) with a total energy of 0.25 mJ at 13.5 nm delivered at 3.33 MHz. As the goal of this investigation is to focus on the fundamental properties of EUV produced plasmas, these conditions were chosen to best illustrate those properties. These EUV pulse conditions are typically shorter and have a higher repetition rate than in commercial EUV lithography systems [22–24]. To make better connection to commercial EUV systems, a limited study was also performed for more industrially relevant conditions, and these results are discussed in Section 5.

The chamber averaged charged particle densities, plasma potential and electron temperature are shown in figure 2 for the first 4 EUV pulses. Plasma properties are shown in figure 3 as a function of position at the beginning and middle of the EUV pulse, and during the inter-pulse period. The quantities shown during the EUV pulse are the rate of photoionization by EUV photons [$S(h\nu)$ cm^{-3} s^{-1}], the density of *in-flight* high energy electrons [e-high energy, cm^{-3}], the rate of ionization by *in-flight* high energy electrons [S(e-high energy) cm^{-3} s^{-1}] and plasma potential [potential, V]. During the inter-pulse period when there are no EUV photons, the photoionization source is replaced by ionization by bulk electrons [S(e-bulk energy) cm^{-3} s^{-1}]. Over the short time addressed by these simulations (1–2 μs) the transport of even light hydrogen ions is not significant, and so losses by diffusion are nominal. The plasma properties are dominated by pulse-to-pulse accumulation of ions and local kinetics, including dissociative recombination.

The chamber averaged plasma densities are a few 10^8 cm^{-3}, however the spatial distribution of plasma density largely follows photoionization by the EUV pulse, as discussed below, commensurate with the measurements and computations of Astakhov *et al* [33]. With the EUV flux expanding spherically outwards and the H_2 being largely transparent to the EUV (little depletion of the EUV flux), the photoionization source scales inversely with the square of the distance from the Sn droplet. At the peak of the EUV photon flux (figures 3, 40 ns), the photoionization source exceeds 4×10^{18} cm^{-3} s^{-1} at the location of the Sn droplet, decreasing to 1×10^{14} cm^{-3} s^{-1} at the radial sidewall. The asymmetry in the photoionization source, skewed towards the IF at the top of the reactor, results from the reflection and focusing of the EUV by the bottom collector mirror. The more intense focused radiation produces locally larger photoionization.

Photoionization produces H_2^+ as the primary ion, which is then rapidly converted to H_3^+ by charge exchange with H_2. With a rate coefficient of 2.6×10^{-9} cm^3 s^{-1} for this process, at a pressure of 10 Pa, the conversion of H_2^+ to H_3^+ occurs in <0.5 μs. H_2^+ is also converted to H^+ by charge exchange with H atoms with a rate coefficient of 6.4×10^{-10} cm^3 s^{-1}. With an on-axis H density exceeding 2.6×10^{11} cm^{-3} after the 5th pulse, the time required for conversion is 5–6 ms, and so would only be important after tens or hundreds of pulses when the H atom density significantly increases. H^+, the secondary ion produced by photoionization, is fairly stable. H^+ is depleted by 3 body reactions to produce H_3^+ (rate coefficient 3.1×10^{-29} cm^6 s^{-1}) which at this pressure requires 5–10 ms. Collisional radiative recombination is slow at these densities and electron temperatures.

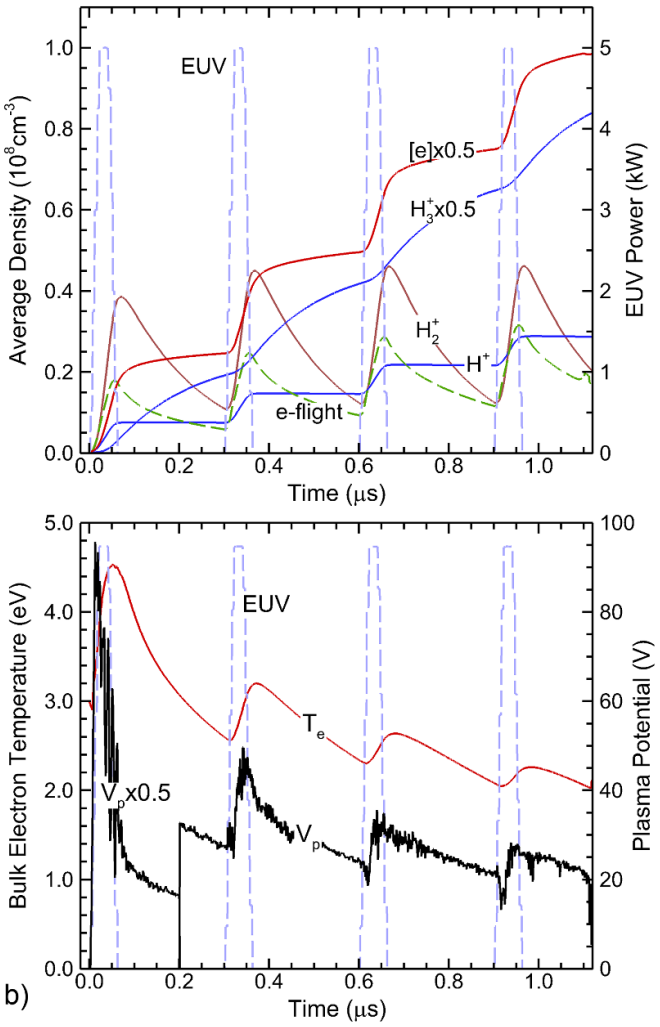

Figure 2. Chamber averaged plasma properties for an H_2 pressure of 10 Pa (75 m Torr). (a) Charged particle densities. (b) Plasma potential and electron temperature.

The high-energy or *in-flight* electrons are those produced by photoionization and secondary emission from surfaces. The *in-flight* electrons are produced on each pulse with fairly constant densities with energies up to 79 eV, after which collisions degrade their energy, or the photoelectrons are lost to surfaces. The densities of *in-flight* electrons shown in figure 3 at the beginning of the 3rd pulse consist mostly of electrons still slowing down from the previous pulse (also shown by the chamber averaged densities in figure 2). With turn-on of the EUV pulse, the high energy *in-flight* electrons are produced in proportion to the local EUV flux, however these photo-electrons quickly transport throughout the reactor to have a more uniform distribution than the EUV flux. The EUV

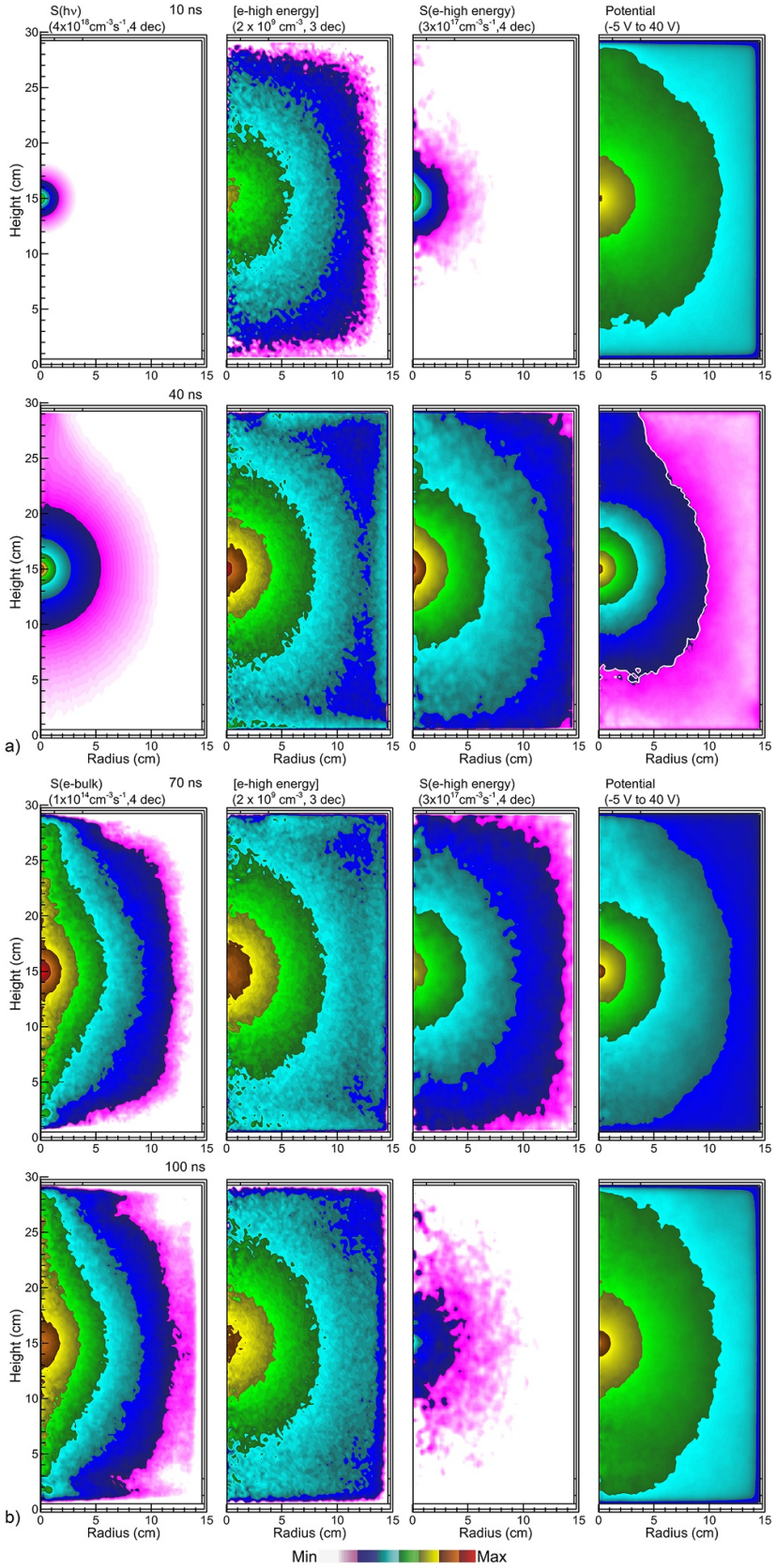

Figure 3. Plasma properties for the 3rd EUV pulse and inter-pulse period. (a) Photoionization source, density of *in-flight* high energy electrons, ionization by *in-flight* high energy electrons and plasma potential at 10 ns and 40 ns. (b) Ionization by bulk electrons, density of *in-flight* high energy electrons, ionization by *in-flight* high energy electrons and plasma potential at 70 ns and 100 ns. Maximum values plotted are noted in each image. The dynamic range in decades are noted for images plotted on a log scale. The color bar indicates the scaling from minimum to maximum values.

flux produces electrons at boundaries of the chamber by photoelectron emission, which introduces negative space charge at the periphery of the reactor. This negative space charge is somewhat mitigated by high energy electrons produced in the periphery of the reactor that are lost to surfaces which result in an incremental positive space charge. Secondary electron emission by the high energy electrons striking surfaces then adds back negative space charge. However, secondary electron emission for electrons, even at 70–80 eV, is small.

The ionization sources are dominated by photoionization, S_{ph}, and by collisions by the high energy *in-flight* electrons, S_{eb}. The rate of photoionization during the pulse is about an order of magnitude larger than S_{eb}. However, integrated over the entire pulse period, 40% of the total volume inventory of ionization is directly attributable to photoionization and 60% results from collisions by the *in-flight* electrons. With some accumulation of *in-flight* electrons from pulse-to-pulse having up to 80 eV of kinetic energy, the photoelectrons produce on average 1–2 additional ionizations.

As discussed by Astakhov *et al* [33], high energy photoelectrons produced early during the first EUV pulses can rapidly escape the chamber, producing a positive space charge. The positive space charge then produces a plasma potential that increases to a sufficiently large value to confine subsequent photoelectrons. The simulations discussed here produce this behavior. At the beginning of the first pulse, photoelectrons are rapidly lost, producing a maximum in the plasma potential at the center of the chamber in excess of 100 V. At this time, the majority of the negative charge is in the form of the *in-flight* electrons, with there being significant positive space charge at the site of the droplet from which photoelectrons are diverging. As the bulk plasma density increases with time and with successive pulses, the positive space charge produced by escaping *in-flight* electrons is progressively shielded by the bulk plasma, with the end result being that the peak plasma potential decreases. With additional pulses and longer interpulse periods, the plasma potential peaks at 25–30 V and asymptotes to about 20 V. There is a commensurate decrease in bulk electron temperature from 4–5 eV at the start of pulsing to about 2 eV after several pulses.

At the beginning of each EUV pulse, there is a dip of several volts in the plasma potential. This dip corresponds to nearly instantaneous photo-electron emission resulting from the EUV illumination of inner surfaces of the chamber which introduces negative space charge to the periphery of the chamber (figures 3, 40 ns). The negative space charge then produces negative plasma potential in the periphery of the reactor of -3 to -5 V, which in turn pulls down the peak plasma potential. The plasma potential remains positive at the periphery of the plasma at the top of the reactor adjacent to the IF and the gas inlet as secondary electron emission (by any method) does not occur from these surfaces. As a result, there is no injection of negative space charge adjacent to those surfaces.

Zhang *et al* performed PIC simulations of EUV generated plasmas in a 1-dimensional spherical geometry with the EUV source at the center and a mirror collector surface as the outer shell [56]. They predict a similar negative plasma potential near the collector surface during the duration of the 100 ns EUV pulse in 1.5 Pa of H_2. Their predicted negative potential is as large as -60 V, significantly more negative than the results here. This more negative plasma potential is attributed to the significantly larger EUV intensity striking their collector surface, producing a proportionally large photo-electron flux returning to the plasma, and lower pressure which results in less back-scatter of photo-electrons into the collector.

After the EUV pulse terminates, the photoionization source ceases as does the source of high energy photoelectrons. (The photoelectron source is replaced by the ionization source by bulk electrons for 70 and 100 ns in figure 3.) The remaining ionization sources are collisions by bulk electrons and by slowing of *in-flight* electrons. The ionization by *in-flight* electrons rapidly decreases as these electrons lose energy through collisions and are not replenished by photoionization. The ionization by bulk electrons has a maximum value of 10^{14} cm^{-3} s^{-1}, which is 3–4 orders of magnitude smaller than by photoionization and by slowing *in-flight* electrons. However, since the ionization source by bulk electrons persists for the entire pulse period, its contribution to the total integrated ionization is about 1%—not a hugely important contribution but also not negligible.

The bulk ionization source is dominantly aligned along the axis, which also corresponds to the spatial distribution of the bulk electron temperature. This distribution is a consequence of the reflection of the EUV from the bottom collector mirror which produces twice the EUV fluence along the axis where the EUV fluxes are already most intense. The contributions to electron heating by slowing *in-flight* electrons is proportionately larger along the axis.

These trends in ionization sources and plasma potential are reflected in the spatially dependent plasma densities. Charged particle densities (electrons, H^+, H_2^+, H_3^+) in the chamber during the 4th EUV pulse and the following interpulse period are shown in figure 4. Negative H^- ions are dominantly produced by dissociative electron attachment to vibrationally excited states of H_2. Although there is significant vibrational excitation of H_2 (densities of $H_2(v=1)$ and $H_2(v=2)$ exceed 10^{11} cm^{-3} on axis), significant densities of H^- are not produced for these conditions and timescales. The negative ion density does not exceed 2×10^8 cm^{-3} in the center of the chamber.

At the beginning of the 4th EUV pulse (10 ns), the electron density is 2×10^{10} cm^{-3} in the center of the chamber, decreasing exponentially to several 10^7 cm^{-3} in the periphery of the reactor. The electron density is skewed along the axis and towards the IF due to the reflection of the EUV from the bottom collector which intensifies photoionization sources in those regions. In spite of the photoionization favoring production of H_2^+, its density prior to the start of the EUV pulse has decreased to 10^9 cm^{-3} in the center of the chamber dominantly due to charge exchange reactions that produce H_3^+ and secondarily by dissociative recombination. The electron density is largely balanced by the density of H_3^+.

At the end of the EUV pulse (70 ns), the electron density exceeds 1×10^{11} cm^{-3} in the center of the reactor, with the majority of this increase being due to production of H_2^+, as indicated by its skewed density which follows the EUV

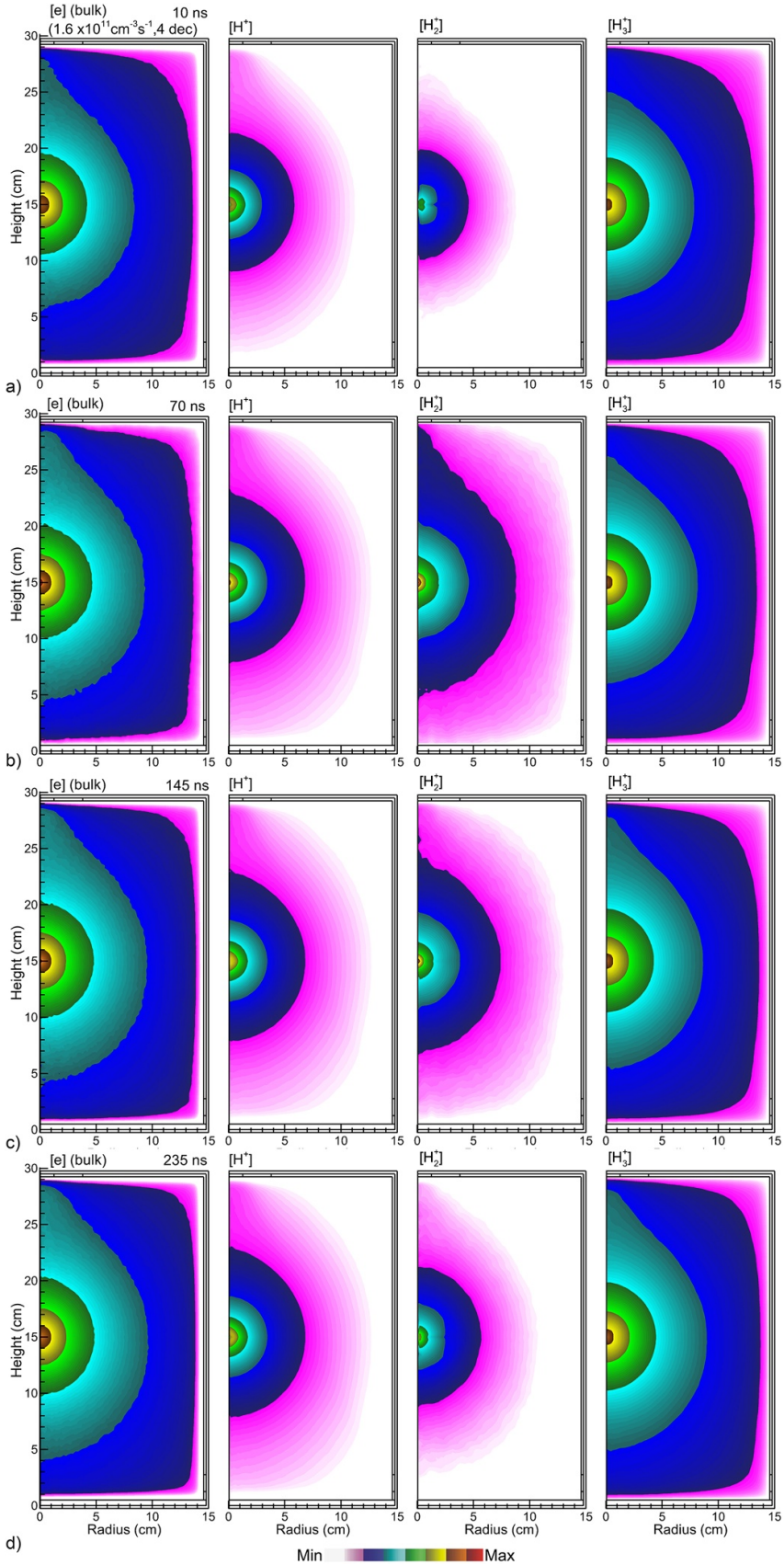

Figure 4. Densities of bulk electrons, H^+, H_2^+ and H_3^+ for the 3rd EUV pulse and afterglow at (a) 10 ns, (b) 70 ns, (c) 145 ns, (d) 235 ns. Images are plotted on a 4-decade log-scale with maximum value of 1.6×10^{11} cm^{-3}.

fluence. During the interpulse period (145 ns, 235 ns) charge exchange depletes H_2^+ while increasing the density of H_3^+. Meanwhile, ambipolar diffusion spreads the charged particle densities throughout the chamber.

With about half the total ionization being produced by high energy, *in-flight* electrons generated by EUV photoionization, the energy distributions and transport of *in-flight* electrons are important to plasma dynamics. EEDs, f(ε), for the high energy *in-flight* electrons are shown in figure 5 during and after the 4th EUV pulse. Values are shown at the midplane of the chamber at radii of 1.5 cm (near the source of EUV radiation), 8 cm (mid-radius) and 14 cm (adjacent to the outer wall).

About 80% of the *in-flight* electrons are initially produced with an energy of 78 eV and 20% are produced with an initial energy of 50 eV. At the beginning of the EUV pulse, the *in-flight* electrons from the prior pulses have largely decayed in energy to below the ionization threshold of H_2.

Focusing first on $f(\varepsilon)$ at a radius (R) of 1.5 cm, at 50 ns near the end of the EUV pulse, the distribution function has maxima at 78 and 50 eV, reflecting the photoionization sources. These maxima are significantly broadened to a maximum energy of nearly 90 eV. Photoelectrons produced at 78 eV at large radii are accelerated towards the center of the chamber due to the positive plasma potential of tens of volts. This results in *in-flight* electrons gaining energy above their initial value due to photoionization. Photoelectrons produced at smaller radii with trajectories radially outwards are slowed by the decreasing plasma potential.

Inelastic collisions of high energy, *in-flight* electrons are largely with H_2 and are dominated by ionization (minimum energy loss 15.4 eV), followed by electronic excitation (minimum loss 11.9 eV) and finally by vibrational excitation (0.5 eV to several eV). When the photoelectron source ceases, the tail of $f(\varepsilon)$ is rapidly depleted by these collisions (75 ns). With the decrease in plasma potential, there is less acceleration of *in-flight* electrons towards the center of the reactor. By 100 ns, the decay in the tail of $f(\varepsilon)$ results in a commensurate decrease in the ionization source by *in-flight* electrons. At later times, the tail of $f(\varepsilon)$ is sustained by electrons accelerated towards the center of the reactor by the positive plasma potential. These dynamics in $f(\varepsilon)$ are similar to those described by Beckers *et al* [33].

The $f(\varepsilon)$ for *in-flight* electrons at a radius of 8 cm has contributions from locally produced photo-electrons and from electrons dominantly produced at smaller radii. With there being a finite time for electrons to transport from remote locations, the high energy tail of $f(\varepsilon)$ at $R = 8$ cm persists for a longer time after the end of the EUV pulse than at the center of the reactor. Ionization by slowing *in-flight* electrons also persists longer at the larger radius. The peaks of $f(\varepsilon)$ at 78 and 50 eV are less broadened to higher energy than at the smaller radius (maximum energy of 83 eV as opposed to 90 eV). The higher than 78 eV electrons are produced by photoelectrons originating at larger radii and being accelerated inwards by the plasma potential. There is simply less plasma potential available at mid-radius than at the center of the chamber, and

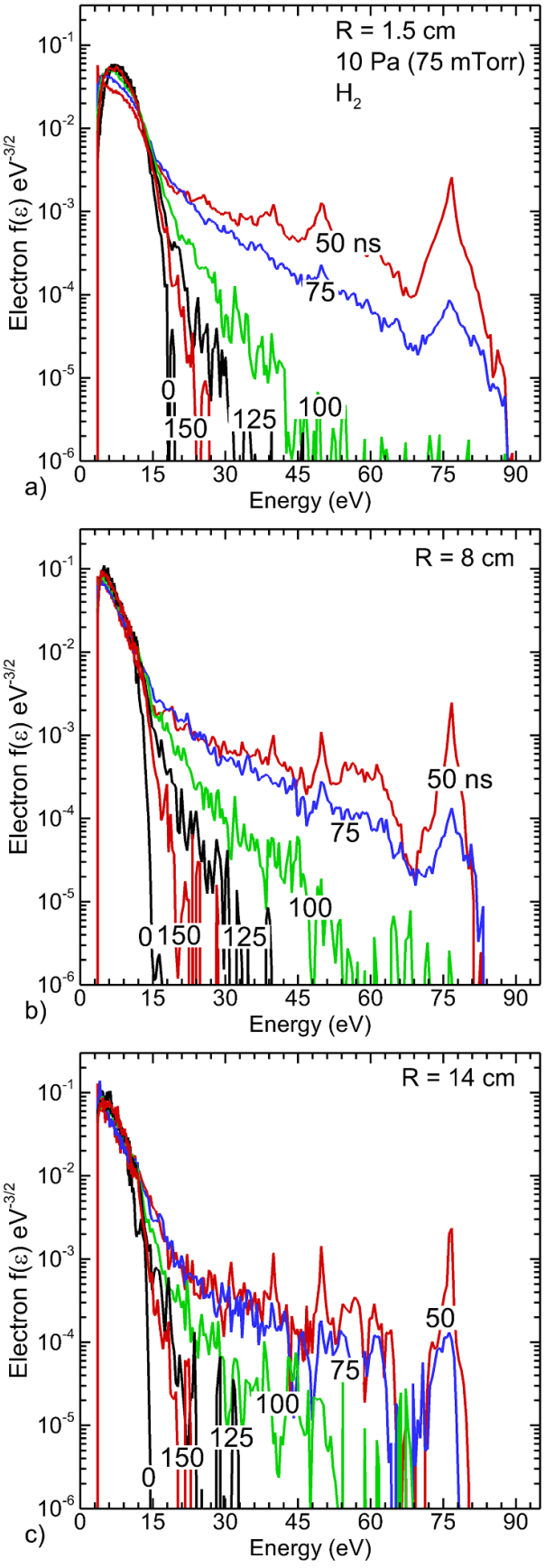

Figure 5. Energy distributions ($eV^{-3/2}$) of *in-flight* electrons at various times during the EUV pulse. The locations are at mid-height in the chamber at radii of (a) 1.5 cm, (b) 8 cm and (c) 14 cm.

so there is less broadening of the initial peak in $f(\varepsilon)$ due to photoionization.

The $f(\varepsilon)$ for *in-flight* electrons at $R = 14$ cm (within 1 cm of the wall) has a more persistent, longer lasting high energy tail than at smaller radii. At $R = 14$ cm, essentially all photoelectrons that are produced with trajectories radially outwards are lost to the walls. The majority of the *in-flight* electrons recorded at $R = 14$ cm with energies less than 78 eV originate from smaller radii. With there being less than a few volts of positive plasma potential (and for some time during the pulse there is a negative plasma potential) at radii greater than $R = 14$ cm, there are few *in-flight* electrons that are accelerated to energies above 78 eV.

The choice of chamber pressure has several tradeoffs. The purpose of the chamber being gas filled is, at least partly, to protect optics from the debris resulting from ablation of the Sn droplet. In this regard, higher pressures are better. The upper limit on chamber pressure is likely that value above which the gas is no longer transparent to the EUV. Until that limit is reached (that is, remaining optically thin), high pressure will equate to more total photoionization by the EUV radiation and so higher initial plasma densities.

Wang *et al* performed PIC simulations of EUV generated plasmas in argon at pressures of 1 and 5 Pa [57]. Although the rates of collisional energy loss of *in-flight* electrons differ in Ar compared to H_2, their simulations show a similar quenching of the tail of the EED, $f(\varepsilon)$, as shown here. For example, at 5 Pa, the tail of $f(\varepsilon)$ having initial energies exceeding 50 eV required up to 500 ns to decrease 10–15 eV.

The chamber averaged densities of bulk electrons, H_3^+, *in-flight* electrons, electron temperature and plasma potential are shown in figure 6 for hydrogen pressures of 5 Pa (37.5 m Torr) to 100 Pa (0.75 Torr) for the first 4 EUV pulses. Spatially dependent plasma properties at the end of the 3rd pulse are shown in figure 7 for pressures of 5, 30 and 100 Pa. The chamber averaged bulk electron densities scale nearly linearly with pressure over this range of pressure (from 1×10^8 cm^{-3} to 1×10^9 cm^{-3}). With there being little depletion of EUV radiation by absorption over this range of pressure, higher pressure directly translates into high rates of photoionization. These pressure dependencies follow the experimental trends of van der Horst *et al* who measured increasing plasma densities with H_2 pressure [58] and calculations by Astakhov *et al* [34].

The peak chamber averaged densities of *in-flight* high energy electrons scale less strongly with pressure. From 5 to 100 Pa, the peak *in-flight* density increases by only a factor of 10 to 10^8 cm^{-3}. This lack of scaling with pressure is due, in part, to the more rapid rate of collisional loss of energy by *in-flight* electrons at higher pressures. At 100 Pa, the *in-flight* electrons have essentially fully thermalized at the end of the interpulse period (300 ns) whereas at 6 Pa, the density of *in-flight* electrons at the end of the interpulse period is nearly 25% that of the peak value.

The spike in plasma potential during the EUV pulse results from high energy *in-flight* electrons that escape the plasma, leaving positive space charge behind. The plasma potential also serves to confine bulk electrons. For example, during the 3rd EUV pulse, the plasma potential peaks at 50 V at 5 Pa, with that maximum decreasing to 12–15 V at 100 Pa. At higher pressures, the inflight electrons are more collisional, thermalize faster and are less likely to leave the plasma. These

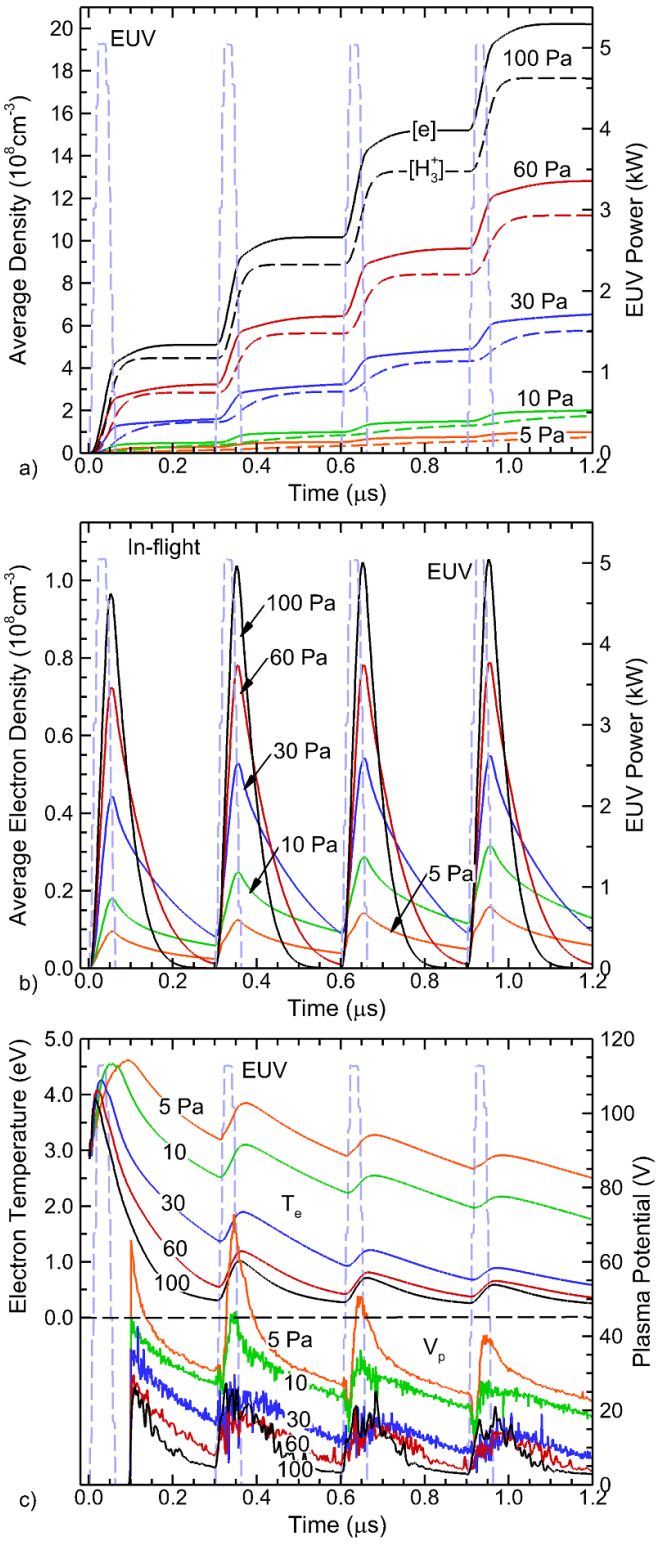

Figure 6. Chamber averaged plasma properties for an H_2 pressures of 5 (37.5 m Torr) to 100 Pa (750 m Torr). (a) Charged particle densities, (b) *in-flight* electron density and (c) Plasma potential and electron temperature.

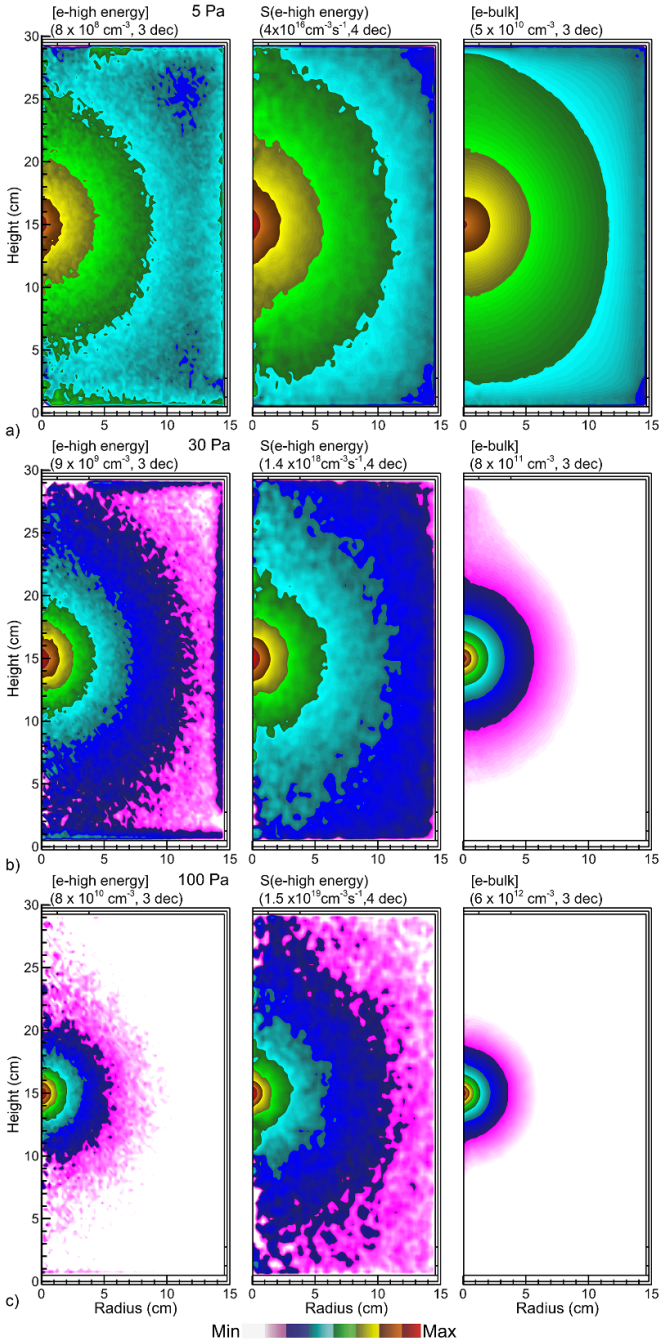

Figure 7. Densities of *in-flight* high energy electrons, ionization source by *in-flight* electrons and densities of bulk electrons at 40 ns (maximum of the EUV pulse) during the 4th pulse. Results are shown for H_2 pressures of (a) 5 Pa (37.5 m Torr), (b) 30 Pa (225 m Torr) and (c) 100 Pa (750 m Torr). Values are plotted on a log scale with the maximum value and dynamic range in decades noted in each figure.

conditions result in less positive space charge generation and so a lower plasma potential. The bulk electron temperature is also lower at higher pressures, thereby requiring a lower plasma potential for confinement.

At the start of the EUV pulse, photoelectron emission at the walls of the chamber introduces negative space charge in the periphery of the reactor, which produces a momentary decrease in plasma potential. The photoelectron emission begins nearly instantly as the EUV pulse turns on whereas the loss of high energy *in-flight* electrons occurs up to tens of ns later. The decrease in plasma potential due to this injection of negative space charge is most evident at 5 Pa and arguably does not occur at 100 Pa. The rate of photoelectron emission is nearly independent of pressure, depending only on the EUV flux striking the walls. At high pressures, the plasma density is larger which results in more efficient shielding, and the rate of collision scattering of the secondary electrons back into the wall is larger. Both of these processes work to minimize the decrease in plasma potential. At low pressures, the secondary electrons are more likely to penetrate into the bulk plasma and there is less shielding due to the lower plasma density.

The bulk electrons are heated by photo-electrons (the *in-flight* electrons) and high energy secondary electrons slowing to energies less than 4–5 eV. At low pressures, the rates of decay in energy of both the *in-flight* and bulk electrons are lower. At 5 Pa, this results in the maximum of the bulk electron temperature T_e, occurring about 50 ns after the end of the EUV pulse and the generation of energetic photo-electrons. The high energy *in-flight* electrons require more time to cascade to lower energies through collisions prior to joining the bulk electron density. At 100 Pa, the maximum in T_e, occurs at the leading edge of the EUV pulse when the heating rate per bulk-electron is the highest. T_e then progressively decreases on a pulse-to-pulse basis. At a given pressure and for a constant EUV pulse energy, the production of energetic *in-flight* electrons is constant, and so the heating rate of bulk electrons by slowing of the *in-flight* electrons is constant. With the bulk electron density increasing from pulse-to-pulse, then the heating rate per electron decreases. In the pulse-periodic steady state the electron temperature at 5 Pa is $T_e = 2.5$–3 eV, and 0.4–0.6 eV at 100 Pa.

The spatially dependent densities of high energy *in-flight* electrons, the ionization produced by *in-flight* electrons and the bulk electron density at the peak of the EUV pulse (40 ns) during the 4th pulse are shown in figure 7. Results are shown for pressures of 5 Pa, 30 Pa and 100 Pa. The maximum *in-flight* electron density increases from 8×10^8 cm^{-3} at 5 Pa to 8×10^{10} cm^{-3} at 100 Pa, a factor of 100. This increase results, in part, from the increase in production of photoelectrons that is afforded by the higher pressure—a factor of 20. The remainder of the increase results from the collisional confinement of the *in-flight* electrons. When normalized by the maximum density at the center of the chamber, at 5 Pa, *in-flight* electrons have a relative density at 10^{-3} of the maximum adjacent to the chamber walls (15 cm). At 100 Pa, these electrons are confined to about 8 cm radius. This greater extent of the *in-flight* electrons at the low pressure is reflected by the ionization sources by *in-flight* electrons (shown extending to 10^{-4} of the maximum in figure 7).

The maximum bulk electron density increases from 5×10^{10} cm^{-3} at 5 Pa to 6×10^{12} cm^{-3} at 100 Pa, a factor of 100. The spatial profile of the EUV photoionization is essentially the same for this range of pressure—only the magnitude of the source changes. This increase in photoionization would account for a factor 20 in the maximum electron density. The

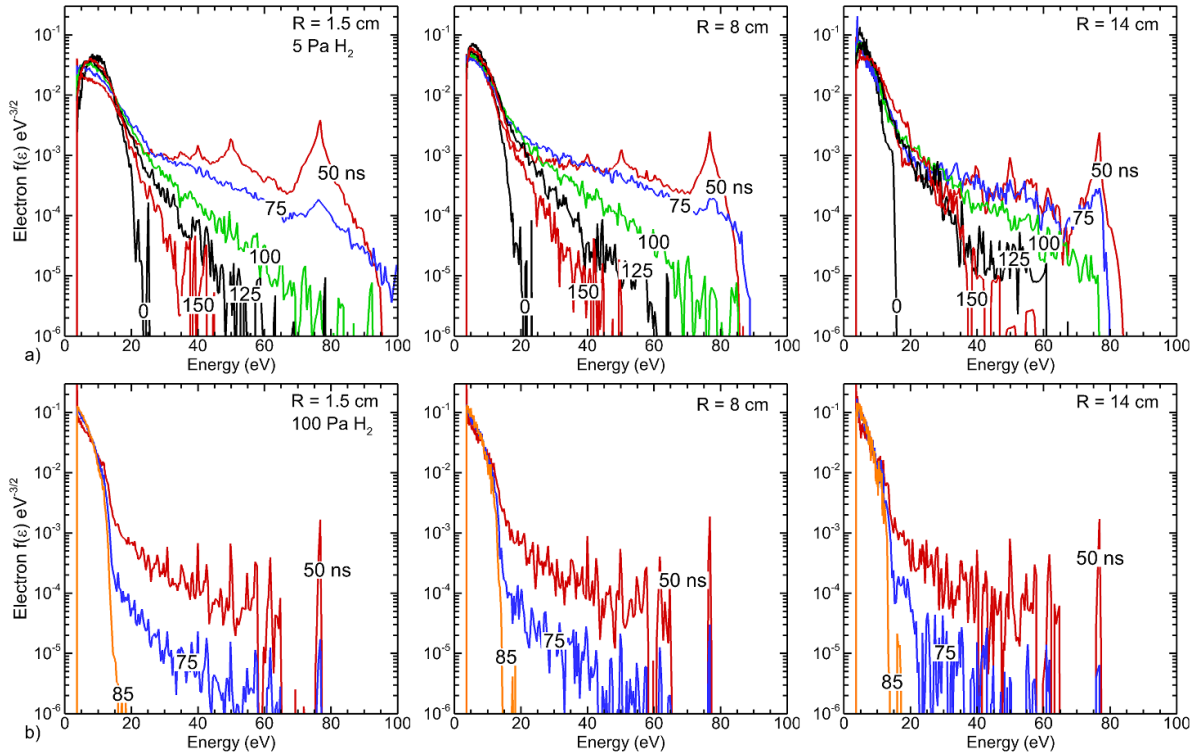

Figure 8. Energy distributions ($eV^{-3/2}$) of *in-flight* electrons at various times during the EUV pulse at mid-height in the chamber for radii of 1.5 cm, 8 cm and 14 cm. Results are shown for H_2 pressures of (a) 5 Pa (37.5 m Torr) and (b) 100 Pa (750 m Torr).

remainder comes from the confinement of the *in-flight* electrons which produces a more confined ionization source and from less diffusional transport of the bulk electrons. At the end of 5 pulsed periods, the inventory of electrons (spatially integrated density) at 5 Pa is 1.8×10^{11} cm^{-3}, and at 100 Pa is 2.5×10^{12} cm^{-3}, a factor of 14 higher. The less than linear scaling of electron density with pressure at the higher pressure results from volume losses by dissociative recombination. With the higher plasmas densities and lower bulk electron temperature, dissociative recombination of H_3^+ and H_2^+ represent significant losses.

The energy distributions of the *in-flight* high energy electrons for pressures of 5 Pa and 100 Pa are shown in figure 8 at mid-height for radii of 1.5, 8, and 14 cm. At the lower pressure, there is long persistence of the high energy tail of $f(\varepsilon)$ due to the lower collisional rate of energy loss. In spite of more rapid loss of photo-electrons to the wall at $R = 14$ cm, the transport of high energy electrons from smaller radii sustains the tail of $f(\varepsilon)$ for nearly 100 ns. At $R = 1.5$ cm, the tail more rapidly decays (on the average, high energy electrons are moving to larger radii) while the peaks in $f(\varepsilon)$ due to photoionization sources (78 eV, 50 eV) are significantly broadened, particularly to high energy. With the larger plasma potential, *in-flight* electrons produced at large radii are accelerated into the center of the reactor, gaining more energy accelerating up the plasma potential.

At 100 Pa, the higher rate of collisional energy loss depletes the high energy tail of $f(\varepsilon)$ within 10–15 ns of the end of the EUV pulse. There is little, if any, broadening of the peak in $f(\varepsilon)$ at 78 eV at the smaller radii. The plasma potential is lower and so there is less energy to gain by *in-flight* electrons produced at larger radii; and as these electrons transport to smaller radii, they are more collisional. At the end of the interpulse period (240 ns) the *in-flight* electrons at all radii have been depleted and largely transitioned to being bulk-electrons.

4. Properties of EUV induced plasma in H_2 with Sn vapor

The discussion to this point has addressed EUV plasma generation in pure H_2. In commercial EUV sources with radiation produced by ablation of Sn droplets, there is Sn debris produced by the ablation. This debris is in the form of energetic ions, low energy Sn vapor and, likely, Sn clusters [59–61]. The purpose of the gas fill of the chamber and gas flow is, in part, to remediate the consequences of the Sn debris and vapor. A 30 μm diameter spherical Sn droplet contains 5×10^{14} atoms. The distribution of these Sn atoms in the chamber depends on the energy and ion state of the ablation products and the gas flow through the chamber that sweeps out the ablation products. These dynamics are beyond the scope of this investigation. To provide insights into the consequences of metal vapor in the chamber on EUV plasma production, we specified a distribution of neutral Sn vapor that corresponds to 10, 30 and 90 Sn droplets 30 μm in diameter that might accumulate over several pulses. The spherical spatial distribution of the Sn vapor used for this investigation is shown in figure 9(b). For the base case of Sn vapor corresponding to 30 droplets, the maximum on-axis Sn density is 7.5×10^{13} cm^{-3}, decreasing

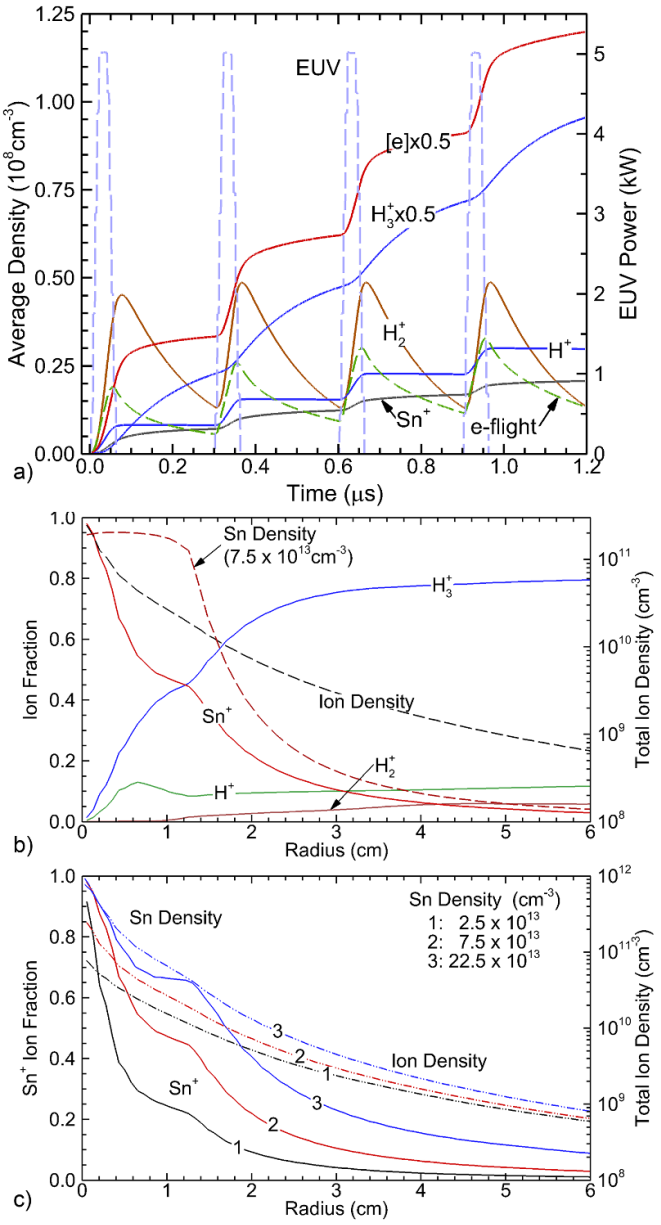

Figure 9. Plasma properties with Sn vapor in the chamber. (a) Chamber averaged charged particle densities for a maximum Sn vapor density of 7.5×10^{13} cm^{-3} (30 droplets). (b) Fraction ion density and total ion density as a function of radius at the end of the 4th interpulse period with Sn vapor from 30 droplets. The relative profile of Sn vapor is shown. (c) Sn^+ ion fraction and total ion density for Sn vapor corresponding to (1) 10, (2), 30 and (3) 90 droplets.

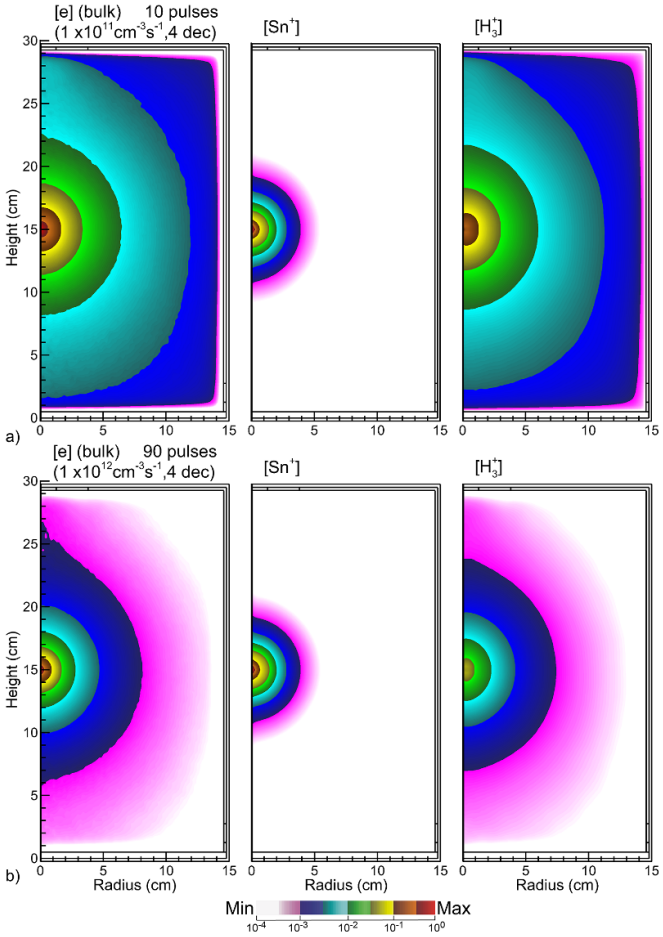

Figure 10. Densities of bulk electrons, Sn^+ and H_3^+ for Sn vapor corresponding to (a) 10 and (b) 90 droplets. Values are plotted on a log scale over 4 decades with the maximum value noted in the image.

as $1/R^2$ for radii greater than about 1 cm. On axis, this density is about 3% of the H_2 density whereas the total inventory of Sn in the chamber is 0.03% that of the H_2.

The reactor averaged charged particle densities with this distribution of Sn vapor are shown in figure 9(a). The ion fractions and total ion density as a function of radius at mid-height in the reactor, and the Sn vapor profile, are shown in figure 9(b). The Sn^+ ion fraction and ion densities for Sn vapor corresponding to 10, 30 and 90 droplets are shown in 9(c). Spatially dependent densities of bulk electrons, Sn^+ and H_3^+ for Sn vapor corresponding to 10 and 90 droplets are shown in figure 10 at the end of the 4th pulsed period.

For the base case of Sn vapor corresponding to 30 droplets, on a reactor averaged basis, Sn^+ accounts for about 15% of the ion density in spite of the Sn inventory being only 0.03% that of the H_2. The reactor averaged electron density increases by about 20% compared to the EUV produced pure H_2 plasma.

This disproportionately large inventory of Sn^+ results from several factors. The photoionization cross section for Sn, 1.1×10^{-17} cm^2, is 170 times that for the total photoionization of H_2 (6.6×10^{-20} cm^2), and so the production of Sn^+ by photoionization is proportionally larger. There is charge exchange from H_n^+ to Sn to produce Sn^+ with rates that are likely close to those given by the Langevin rate coefficient. For otherwise equal conditions, photoionization produces more Sn^+ ions while those H_n^+ ions that are produced will be depleted by charge exchange with Sn vapor. For our conditions, the Sn vapor has its maximum density where the EUV flux is the highest, which disproportionately produces Sn^+ compared to the uniformly distributed H_2. These trends are shown by the ion fraction as a function of radius and total ion density at the

end of the interpulse period in figure 9(b). On axis, the Sn^+ fraction of all ions is nearly unity. At larger radii where the Sn vapor density decreases, there is a proportional decrease in the ion fraction of Sn^+ and increase in the ion fraction of H_n^+, again dominated by H_3^+.

Ion fraction of Sn^+ and total ion density are shown in figure 9(c) for notionally Sn vapor corresponding to the ablation of Sn droplets by 10 (on-axis density 2.5×10^{13} cm^{-3}), 30 (7.5×10^{13} cm^{-3}) and 90 (22.5×10^{13} cm^{-3}) EUV pulses. These results are shown at the end of the 4th interpulse period. The relative profile of the Sn vapor is the same as shown in figure 9(b). The on-axis electron density increases by about factor of 10 (7.7×10^{10} cm^{-3} to 8.4×10^{10} cm^{-3}) corresponding to the increase in the on-axis density of the Sn vapor. The total volume integrated inventory of electrons increases by about 60% with the increase in Sn vapor. For the higher Sn vapor density, the ion fraction is dominated by Sn^+ to a radius of 1.7 cm.

With the increase in Sn vapor, the plasma density becomes more tightly focused at the center of the chamber, as shown in figure 10, as a consequence of the photoionization of the Sn. At the higher Sn vapor density, there is significant depletion of H_3^+ at the center of the chamber resulting from charge exchange from H_n^+ to Sn. The photoionization of Sn at the higher range of densities investigated here results in a minor amount of depletion (about 1.2%) of the EUV flux delivered to the IF.

5. Properties of EUV induced plasma in H_2 for industrial-like conditions

Commercial EUV sources using Sn vapor ablation operate at repetition rates of 50–60 kHz and H_2 pressures of up to approximately 1 Torr with EUV powers of up to 600 W [22–24]. The plasma produced by these pulses reach a pulse-periodic steady state. The simulations discussed up to this point have emphasized operating conditions that enable fundamental physics to be optimally investigated while remaining computationally tractable.

With the goal of addressing more industrially relevant conditions, simulations of multiple pulses approaching the pulse-periodic state were performed. EUV produced plasmas were simulated in pure H_2 for pressures of 10, 30 and 90 Pa. The EUV pulse repetition rate was 50 kHz, with a pulse length of 1 μs and peak power of 16.7 kW (15 mJ $pulse^{-1}$). The quasi-steady state was achieved in 14–15 pulses with the exception of the density of H atoms and vibrationally excited hydrogen molecules [H_2(v1), H_2(v2), H_2(v3), whose sum is referred to as H_2(v)] which continued moderate increases in density after 15 pulses.

The EUV pulse length was sufficiently long that the majority of energetic photo-electrons thermalized during the EUV pulse. In acknowledgement, during every call to the EETM, the trajectories of energetic photo-electrons were followed to their joining the bulk electron density. The space charge produced by *in-flight* electrons was then restricted to their charged flux entering the bulk distribution. This approximation likely underestimates the positive plasma potential excursion that occurs at the leading edge of the EUV pulses.

The average charged particle densities, peak plasma potential, electron temperature and fluxes to the collector are shown in figure 11. Upon starting the EUV pulse train, the plasma potential peaks to more than 90 V due to loss of energetic photoelectrons to surfaces. The peak electron temperature is more than 4.2 eV. With the longer EUV pulse length and higher EUV power compared to prior pulses, the chamber averaged electron density reaches a pulse-periodic maximum of 5×10^{10} cm^{-3} of which 2/3 is balanced by H_3^+ and 1/3 by H^+. The maximum electron density at the center of the reactor at the source of EUV is 9.1×10^{12} cm^{-3}. The periodic decrease in ion density is dominantly due to recombination of H_3^+. With the pulse periodic loss of energetic photo-electrons become a progressively smaller fraction of the increasing plasma density, the maximum and plasma potential end electron temperature decrease over time. In the pulse-periodic steady state, the maximum in plasma potential is 5.3 V and maximum in average electron temperature is 0.35 eV. The maximum electron temperature at the center of the reactor at the source of EUV is 0.65 eV.

The ion fluxes to the collector (figure 11(c)), dominated by H_3^+, have a pulse periodic maximum of 10^{15} $cm^{-2}s^{-1}$. The oscillation of the ion fluxes to the collector over the pulse period is about a factor of 10. This large oscillation results from two factors. First, there is oscillation in the plasma potential which produces the ambipolar electric fields that accelerate ions into the surfaces. Second, there is significant ionization produced adjacent to the collector by energetic photo-electrons emitted from the surface. (See figure 3(a)) These locally produced ions rapidly drift to the adjacent surface. The flux of H atoms to the collector oscillates from $0.8–1.0 \times 10^{16}$ $cm^{-2}s^{-1}$. The majority of this oscillation is due to H atoms produced adjacent to the surface. The energetic photo-electrons emitted by the surface produce electron impact dissociation of H_2. The rapid charge exchange reaction of H_2^+ produced adjacent to the surface producing H_3^+ also generates an H atom. Recombination of H_3^+ and H^+ on the collector both produce H atoms at the surface.

Measurements of ion fluxes by van de Kerkhof *et al* from an EUV generated H_2 plasma show a similar build-up to a steady state [62]. An EUV source operating at 50 kHz at pressures up to 10 Pa required 30–40 pulses to achieve a pulse-periodic steady state. During a single EUV pulse in the quasi-steady state for a 250 W source, ion fluxes leaving the plasma peaked at 4.5×10^{14} cm^{-2} s^{-1}, decaying to 0.5×10^{14} cm^{-2} s^{-1} prior to the next pulse. Predictions here for ion fluxes striking the collector are commensurate to these measurements in the low pressure regime. In their PIC simulations of EUV produced plasmas in Ar at 5 Pa, Wang *et al* predicted that 12–13 pulses are required to achieve the pulse-periodic steady state [57].

The flux of vibrationally excited H_2 (dominated by $H_2(v = 1)$ to the collector is in excess of 2×10^{16} cm^{-2} s^{-1}. With the vibrational quantum of H_2 being 0.55 eV and assuming unity probability for quenching on the surface the nearly constant $H_2(v)$ flux delivers about 2 mW cm^{-2} to the collector. Given the pulse-periodic ion flux, there is arguably

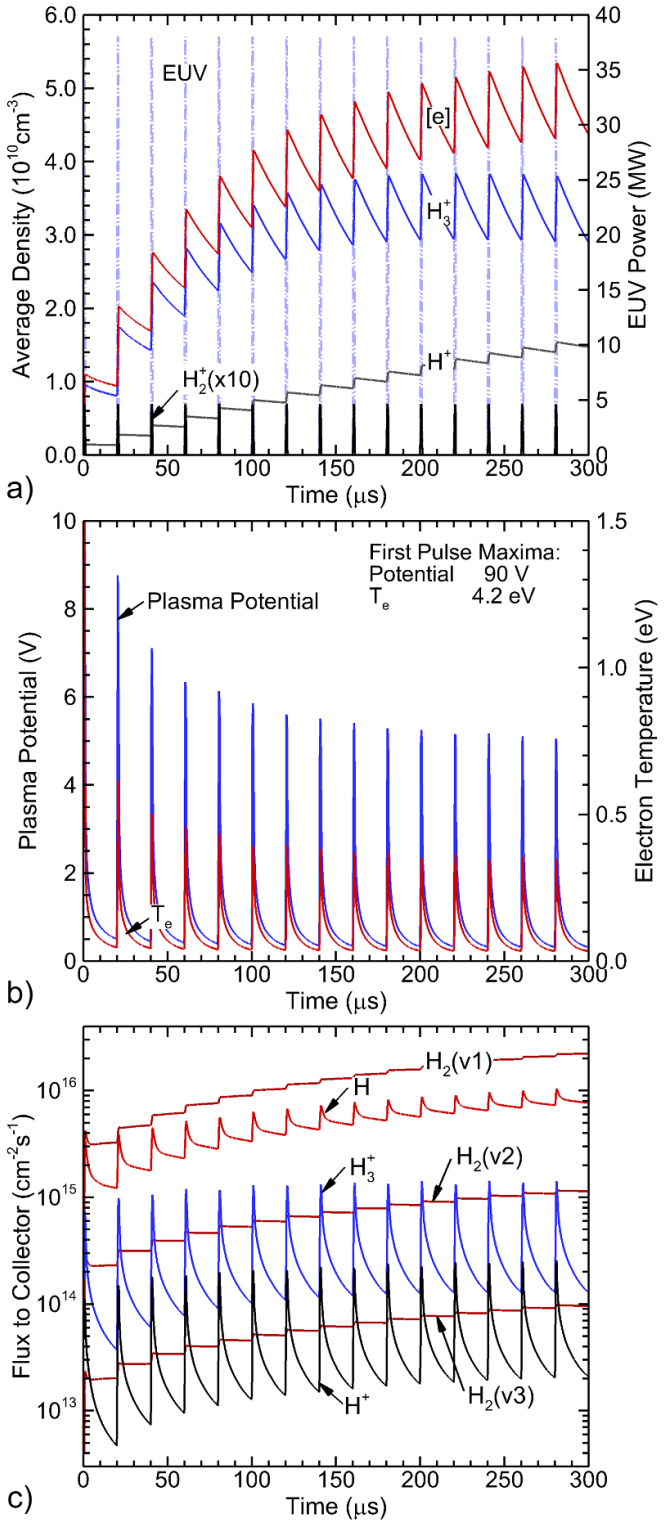

Figure 11. Plasma properties as a function of time for an EUV produced plasma in 30 Pa H_2 for a repetition rate of 50 kHz, EUV pulse of 1 μs with peak power of 16.7 kW. (a) Chamber averaged charged particle densities and EUV power, (b) maximum plasma potential and average electron temperature and (c) average fluxes of charged and neutral species to the collector.

commensurate if not more power delivered to the collector in the form of vibrational states than by recombination of ions. The power delivered to the collector as H atoms would depend on their recombination probability. For example, for a H recombination probability of 0.05 on the collector with the H_2(X) bond energy being 4.5 eV, a flux of 8×10^{15} cm^{-2} s^{-1} delivers 0.3 mW cm^{-2}.

Average electron densities, and fluxes of neutrals and ions to the collector are shown in figure 12 for H_2 pressures of 20, 30 and 90 Pa. The general trend of higher plasma densities and fluxes at higher pressures applies at the lower repetition rate and higher EUV powers investigated in this section. Both charged particle densities and fluxes to the collector have greater modulation over time at higher pressures. The production of surface adjacent species by photo-electron emission and production of H by recombination of ions are both greater at the higher pressure.

6. Concluding remarks

EUV lithography systems based on the ablation of liquid metal droplets to produce radiation must manage the metal vapor and debris resulting from the ablation to prevent damage to optical components. Filling the chamber with low pressure hydrogen gas is one such remediation technique. The transport of EUV radiation through H_2 and metal vapor produces a plasma. In this paper, the characteristics of the EUV generated plasmas in H_2 and H_2/Sn ambient gases (5 Pa to 100 Pa) were discussed based on results from a computational investigation.

The EUV photoionization produces energetic electrons with initial energies up to 78 eV that transport through the gas and slow by collisions, producing additional ionization and dissociation. The contributions to the total inventories of electrons and H atoms produced by the slowing energetic *in-flight* electrons are commensurate or larger than the original photoionization. To achieve more uniform plasma and H-atom production, the operating conditions should be chosen to optimize the transport of *in-flight* electrons, which generally occurs at lower pressures.

At the start of the EUV pulses when the plasma potential is small, energetic photoelectrons escape the plasma, producing positive space charge that supports spikes in the plasma potential of 50–100 V. As the plasma density increases following several EUV pulses, the fractional amount of charge produced by escaping photoelectrons decreases, and the spikes in plasma potential decrease. Energetic photo-electrons continuously escape the plasma at the periphery of the plasma due to the locally low plasma potential. At the same time, significant negative space charge is introduced into the periphery of the chamber by photoelectron emission by EUV radiation striking surfaces, and secondary electron emission by both the energetic inflight electrons and ions. Due to this local negative space charge, the electrical potential at the periphery of the reactor is at times negative. The positive spikes in plasma potential produce energetic ions which strike surfaces. To minimize the energy of ions striking surfaces, conditions should be chosen that minimize the spikes in plasma potential. This could be accomplished by maintaining a high plasma density at the start of the EUV pulse (e.g. high repetition rate of the

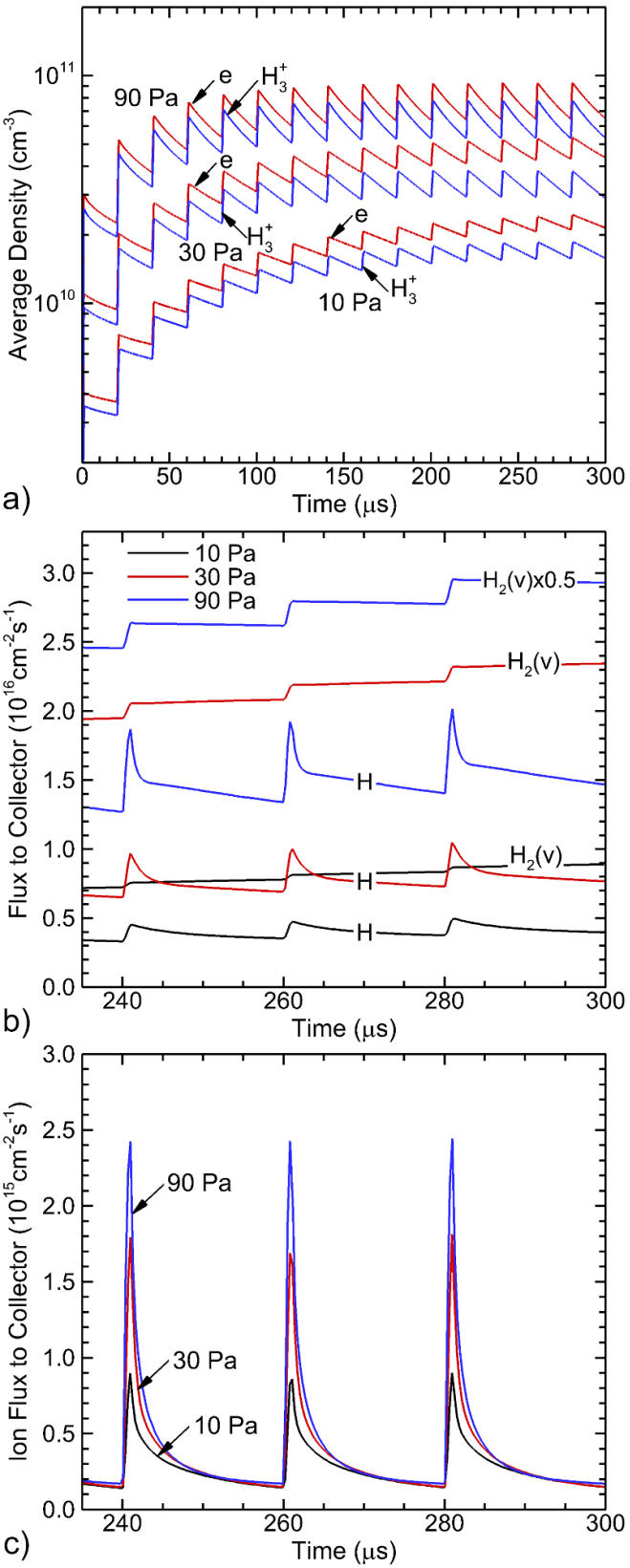

Figure 12. Plasma properties as a function of time for EUV produced plasmas in 10, 30 and 90 Pa H_2 for a repetition rate of 50 kHz, EUV pulse of 1 μs with peak power of 16.7 kW. (a) Chamber averaged densities of electrons and H_3^+. (b) Fluxes of H atoms and vibrationally excited H_2 and (c) total ions to the collector.

EUV pulses) or by shaping the EUV pulse (e.g. a longer ramp-up time of EUV) that would more gradually produce the *in-flight* electrons.

The presence of a small amount of metal vapor can significantly change the ionization balance in the chamber. For example, in pure H_2, the dominant ion after the EUV pulse is H_3^+. Due to the significantly larger EUV photoionization cross section of Sn compared to H_2, and charge exchange of H_n^+ to Sn, the dominant ion may be Sn^+ for metal vapor fractions of less than a few percent. With the rate of ambipolar diffusion and rate of recombination of Sn^+ being significantly lower than that of H_3^+, a large fraction of Sn^+ would result in a more persistent and long-lived plasma. Given that Sn is a potential contaminant of plasma-facing-materials, maintaining a high Sn^+ may not be desirable. However, any higher molecular weight impurity with a larger EUV photoionization cross section and an ionization potential lower than H_n^+ would also produce a more persistent plasma.

This article is part of the *Special Issue of PSST in Memory of Prof. William G (Bill) Graham (1949-2025).* Bill was an excellent scientist and supreme mentor who was extremely generous in serving the profession on many levels. The author MJK worked most closely with Bill in their roles as members of the editorial board and editors in chief of PSST. In these roles, Bill's focus was on improving the journal, while also being focused on best serving the needs of the readership and of the authors. This he accomplished with enthusiasm. It was rare that Bill spoke of his own accomplishments, while being more than happy to celebrate the accomplishments of his colleagues. He was, and continue to be, a true role model for the field of low temperature plasmas.

Data availability statement

The data that support the findings of this study are contained within this paper and available from the corresponding author upon reasonable request.

Acknowledgments

This work was supported by Samsung Electronics Ltd.

Conflict of interest

The authors have no conflicts of interest.

ORCID iD

Mark J Kushner 0000-0001-7437-8573

References

[1] Chen Y, Shu Z, Zhang S, Zeng P, Liang H, Zheng M and Duan H 2021 *Int. J. Extreme Manuf.* **3** 032002
[2] Yang P-S, Cheng P-H, Kao C R and Chen M-J 2016 *Sci. Rep.* **6** 29625

[3] Guo D *et al* 2016 *2016 IEEE Symp. on VLSI Technology* vol 1
[4] Allen N S 2010 *Photochemistry and Photophysics of Polymer Materials* (Wiley)
[5] Wittekoek S 1994 *Microelectron. Eng.* **23** 43
[6] Vollenbroek F A and Geomini M J H J 1988 *Proc. SPIE* **0920** 419
[7] Ishimaru T, Matsuura S, Seki M, Fujii K, Koizumi R, Hakataya Y and Moriya A 2005 *Proc. SPIE* **5754** 1260
[8] Sharma E, Rathi R, Misharwal J, Sinhmar B, Kumari S, Dalal J and Kumar A 2022 *Nanomaterials* **12** 2754
[9] Pirati A *et al* 2016 *Proc. SPIE* **9776** 97760A
[10] Bakshi V 2006 *EUV Lithography* (SPIE Press)
[11] Hoffman J R, Bykanov A N, Khodykin O V, Ershov A I, Fomenkov I V, Partlo W N and Myers D W 2005 *Proc. SPIE* **5751** 892
[12] Horne S F, Niell F M, Partlow M J, Besen M M, Smith D K, Blackborow P A and Gustafson D 2009 *Proc. SPIE* **7271** 72713A
[13] Fu N, Liu Y, Ma X and Chen Z 2019 *J. Microelectron. Manuf.* **2** 19020202
[14] Schoolov K 2022 ASML is the only company making the $200 million machines needed to print every advanced microchip. Here's an inside look (available at: www.cnbc.com/2022/03/23/inside-asml-the-company-advanced-chipmakers-use-for-euv-lithography.html)
[15] Kieft E R, van der Mullen J J J A M, Kroesen G M W, Banine V and Koshelev K N 2005 *Phys. Rev. E* **71** 26409
[16] Radamson H H, Simeon E, Luo J and Wang G 2018 *CMOS Past, Present and Future* vol 19, ed H H Radamson, J Luo, E Simoen and C Zhao (Woodhead Publishing)
[17] Ober C K, Xu H, Kosma V, Sakai K and Giannelis E P 2018 *Proc. SPIE* **10583** 1058306
[18] Mizoguchi H *et al* 2016 Development of 250W EUV light source for HVM lithography *In 2016 China Semiconductor Technology Int. Conf. (CSTIC)* (*Shanghai, China, 13–14 March 2016*) (IEEE) pp 1–4
[19] Graeupner P, Kuerz P, Stammler T, van Schoot J and Stoeldraijer J 2022 *Proc. SPIE* **12051** 1205102
[20] Tomuro H *et al* 2023 *Proc. SPIE* **12494** 355–65
[21] Hummler K *et al* 2024 *Proc. SPIE* **12953** 129530V
[22] Medvedev V V, Yakshin A E, van de Kruijs R W E, Krivtsun V M, Yakunin A M, Koshelev K N and Bijkerk F 2012 *Opt. Lett.* **37** 1169
[23] Umstadter K, Graham M, Purvis M, Schafgans A, Stewart J, Mayer P and Brown D 2023 *Proc. SPIE* **12494** 124940Z
[24] Mizoguchi H, Nakarai H, Usami Y, Kakizaki K, Fujimoto J and Saitou T 2022 *Proc. SPIE* **12292** 122920X
[25] Gielissen K 2009 The nature and characteristics of particles produced by EUV sources *PhD Dissertation* Eindhoven University of Technology (https://doi.org/10.6100/IR653353)
[26] Ueno Y, Yanagida T, Suganuma T, Komori H, Sumitani A and Endo A 2009 *Proc. SPIE* **7361** 73610X
[27] Klunder D J W, van Herpen M M J W, Banine V Y and Gielissen K 2005 *Proc. SPIE* **5751** 943
[28] Wu T, Wang X, Lu H and Lu P 2012 *J. Phys. D: Appl. Phys.* **45** 475203
[29] Abramenko D B, Spiridonov M V, Krainov P V, Krivtsun V M, Astakhov D I, Medvedev V V, van Kampen M, Smeets D and Koshelev K N 2018 *Appl. Phys. Lett.* **112** 164102
[30] Elg D T, Panici G A, Liu S, Girolami G, Srivastava S N and Ruzic D N 2018 *Plasma Chem. Plasma Proc.* **38** 223
[31] van Herpen M M J W, Klunder D J W, Soer W A, Moors R and Banine V 2010 *Chem. Phys. Lett.* **484** 197
[32] van den Bos R A J M, Lee C J, Benschop J P H and Bijkerk F 2017 *J. Phys. D: Appl. Phys.* **50** 265302
[33] Beckers J, van de Ven T, van der Horst R, Astakhov D and Banine V 2019 *Appl. Sci.* **9** 2827
[34] Astakhov D I *et al* 2016 *J. Phys. D: Appl. Phys.* **49** 295204
[35] van de Ven T H M, Reefman P, de Meijere C A, van der Horst R M, van Kampen M, Banine V Y and Beckers J 2018 *J. Appl. Phys.* **123** 063301
[36] Mao Q, Gong X, Lu Q, Song Y, Wang D, Bai Y and Ma T 2022 *J. Appl. Phys.* **131** 233301
[37] Elg D T, Sporre J R, Panici G A, Srivastava S N and Ruzic D N 2016 *J. Vac. Scie. Tech nol. A* **34** 021305
[38] Ugur D, Storm A J, Verberk R, Brouwer J C and Sloof W G 2012 *Chem. Phys. Lett.* **552** 122
[39] Braginsky O V *et al* 2012 *J. Appl. Phys.* **111** 093304
[40] Kushner M J 2009 *J. Phys. D: Appl. Phys.* **42** 194013
[41] Krüger F, Lee H, Nam S K and Kushner M J 2022 *J. Vac. Scie. Tech nol. A* **41** 013006
[42] Wang X, Lee H, Nam S K and Kushner M J 2021 *J. Vac. Sci. Tech nol. A* **39** 063002
[43] Kossmann H, Schwarzkopf O, Kammerling B, Braun W and Schmidt V 1989 *Phys. B: At. Mol. Opt. Phys.* **22** L411
[44] Chung Y, Lee E-M, Masuoka T and Samson J A R 1993 *J. Chem. Phys.* **99** 885
[45] Dujardin G, Besnard M J, Hellner L and Malinovitch Y 1987 *Phys. Rev. A* **35** 5012
[46] Dunn G H and Kieffer L J 1963 *Phys. Rev.* **132** 2109
[47] Lysaght M, Kilbane D, Murphy N, Cummings A, Dunne P and O'Sullivan G 2005 *Phys. Rev. A* **72** 14502
[48] Henke B L, Smith J A and Attwood D T 1977 *J. Appl. Phys.* **48** 1852
[49] Day R H, Lee P, Saloman E B and Nagel D J 1981 *J. Appl. Phys.* **52** 6965
[50] Purvis C K 1979 *NASA Technical Memorandum* **79299**
[51] Volynets V, Barsukov Y, Kim G, Jung J-E, Nam S K, Han K, Huang S and Kushner M J 2020 *J Vac. Sci. Technol. A* **38** 023007
[52] Drexel H, Senn G, Fiegele T, Scheier P, Stamatovic A, Mason N J and Märk T D 2001 *J. Phys. B* **34** 1415
[53] Janev R K 1987 *Elementary Processes in Hydrogen-Helium Plasmas: Cross Sections and Reaction Rate Coefficients* (Springer)
[54] Umer H, Ralchenko Y, Bray I and Fursa D V 2023 Electron scattering cross sections for the ground and excited states of tin *At. Data Nucl. Data Tables* **154** 101586
[55] Turulski J and Niedzielski J 1994 *Int. J. Mass Spect. Ion Proc.* **139** 155
[56] Zhang Y, Yu X and Ye Z 2024 *Plasma Sci. Technol.* **26** 085503
[57] Wang X, Chen Z, Chen Z, Wang Y, Wang H, Chen Z, Jiang W and Zhang Y 2025 *Phys. Scr.* **100** 095602
[58] van der Horst R M *et al* 2016 *J. Phys. D: Appl. Phys.* **49** 145203
[59] Nakamura D, Akiyama T, Okazaki K, Tamaru K, Takahashi A and Okada T 2008 *J. Phys. D: Appl. Phys.* **51** 245210
[60] Fujimoto J, Hori T, Yanagida T and Mizoguchi H 2012 *Phys. Res. Int.* **2012** 249495
[61] Rollinger B, Morris O, Chokani N and Abhari R S 2010 Tin ion and neutral dynamics within an LPP EUV source *Proc. SPIE* **7636** 1017–26
[62] van de Kerkhof M, Yakunin A M, Kvon V, Cats S, Heijmans L, Chaudhuri M and Asthakov D 2021 *J. Micro/Nanopattern. Mats. Metro.* **20** 013801